ARTICLES

Quantum spin liquid emerging in two-dimensional correlated Dirac fermions

Z. Y. Meng[1], T. C. Lang[2], S. Wessel[1], F. F. Assaad[2] & A. Muramatsu[1]

At sufficiently low temperatures, condensed-matter systems tend to develop order. A notable exception to this behaviour is the case of quantum spin liquids, in which quantum fluctuations prevent a transition to an ordered state down to the lowest temperatures. There have now been tentative observations of such states in some two-dimensional organic compounds, yet quantum spin liquids remain elusive in microscopic two-dimensional models that are relevant to experiments. Here we show, by means of large-scale quantum Monte Carlo simulations of correlated fermions on a honeycomb lattice (a structure realized in, for example, graphene), that a quantum spin liquid emerges between the state described by massless Dirac fermions and an antiferromagnetically ordered Mott insulator. This unexpected quantum-disordered state is found to be a short-range resonating valence-bond liquid, akin to the one proposed for high-temperature superconductors: the possibility of unconventional superconductivity through doping therefore arises in our system. We foresee the experimental realization of this model system using ultra-cold atoms, or group IV elements arranged in honeycomb lattices.

The quantum mechanical description of the relativistic electron was attained by Dirac, who revealed both its intrinsic angular momentum (spin, which has a half-integer quantum number, $S = 1/2$) and the existence of its antiparticle, the positron[1]. Both obey Fermi–Dirac statistics, which implies that two identical particles cannot occupy the same quantum mechanical state. Such particles are generically called fermions. In the case of vanishing rest mass, the energy of a Dirac fermion is a linear function of momentum. Such massless Dirac fermions were recently observed in two-dimensional solid-state systems such as graphene[2,3] and the surfaces of bismuth-based compounds[4,5]. In graphene, which is a single layer of carbon atoms with a honeycomb structure, unusual electronic behaviour is anticipated, and partly verified experimentally, owing to the two-dimensional Dirac-like dispersion of the electrons at low energies[6]. The interplay of relativistic dispersion with interactions at half-filling is expected to lead to a quantum phase transition between a semimetallic state at low interaction strength and a Mott insulating state at high interaction strengths[7,8]. A Mott insulating state is one that results not from the band structure alone but is due to the effects of interactions. Such correlation effects can be seen using the Hubbard model in its most basic form, as exemplified in high-temperature superconductivity[9], and using ultracold fermionic atoms in optical lattices[10,11]. Studies of Hubbard-like models on the honeycomb lattice suggested the emergence of exotic phases such as gapless spin liquids[12,13], charge density waves[14], quantum spin Hall states[14,15] and superconductivity[16] at or near a density of one fermion per site (half-filling for the two-species case).

Given the various phases proposed for fermions on the honeycomb lattice on the basis of Hubbard-like models, it is important to explore the ground-state properties in the intermediate coupling regime of the original lattice model using an unbiased method. Owing to the absence of a sign problem in determinantal quantum Monte Carlo (QMC) simulations (Methods) in the half-filled case, it is the method of choice for extrapolations to the thermodynamic limit (TDL) and leads to essentially exact results limited only by the statistical noise. Using large-scale quantum Monte Carlo simulations of the spin-1/2 Hubbard model at half-filling on the honeycomb lattice, we show that for intermediate interaction strengths a gapped, non-magnetic phase destroys the semimetal before the transition to an antiferromagnetically ordered Mott insulator at high interaction strengths sets in. This quantum spin-liquid phase is characterized by local correlations that correspond to a resonating valence-bond (RVB) state[17,18], as proposed in the context of high temperature superconductivity[9,19,20].

Since they were originally proposed[17–20], spin-liquid states have been established in effective models of singlet dynamics such as quantum dimer models[21–23]. Our results show that RVB states are realized in a microscopic model of correlated electrons, which is an advance towards their observation in experiments. Honeycomb lattices of group IV elements[24] and ultracold fermionic atoms in optical lattices[10,11,25] seem to be promising candidate systems in which to realize the RVB state using Dirac fermions.

Phase diagram from QMC simulation

Previous numerical studies of the Hubbard model on the honeycomb lattice[26,27] suggested that a single quantum phase transition separates the weak-coupling, paramagnetic semimetal phase from a strong-coupling, antiferromagnetic Mott insulator. When the repulsion is sufficiently strong, antiferromagnetism is possible because the honeycomb lattice is bipartite, meaning that antiferromagnetic order is not geometrically frustrated. However, the honeycomb lattice has the smallest coordination number in two dimensions, such that the effect of quantum fluctuations is the strongest. Hence, the competition between the tendency to order and quantum fluctuations requires a detailed analysis of correlations and a careful extrapolation to the TDL to characterize the possible phases. Here we present results based on projective (temperature $T = 0$) determinantal QMC simulations in the canonical ensemble at half-filling. To assess the emergence of the exotic phases[12–16] mentioned above, we focus in particular on the region near the Mott transition.

The Hamiltonian of the spin-1/2 Hubbard model on the honeycomb lattice equals

[1]Institut für Theoretische Physik III, Universität Stuttgart, Pfaffenwaldring 57, 70550 Stuttgart, Germany. [2]Institut für Theoretische Physik und Astrophysik, Universität Würzburg, Am Hubland, 97074 Würzburg, Germany.

$$H = -t \sum_{\langle i,j\rangle,\alpha} (c^{\dagger}_{i\alpha} c_{j\alpha} + c^{\dagger}_{j\alpha} c_{i\alpha}) + U \sum_{i} n_{i\uparrow} n_{i\downarrow}$$

where $c^{\dagger}_{i\alpha}$ and $c_{i\alpha}$ respectively denote the creation and annihilation operators for spin-up ($\alpha = \uparrow$) and spin-down ($\alpha = \downarrow$) fermions on lattice site i, $n_{i\alpha} = c^{\dagger}_{i\alpha} c_{i\alpha}$, t denotes the nearest-neighbour hopping amplitude and $U \geq 0$ denotes the strength of the on-site repulsion. The first summation runs over all nearest-neighbour pairs, as denoted by $\langle i, j\rangle$ (and both spins). Our notation for points and vectors in real and momentum space is shown in the inset of Fig. 1. At $U = 0$, the tight-binding Hamiltonian has a linear dispersion near the Dirac points (K and K'; see inset of Fig. 1), where the conduction and valence bands touch at half-filling, corresponding to a density $\sum_{\alpha}\langle n_{i\alpha}\rangle = 1$. At half-filling, the finite-U region can be studied using projective QMC to obtain ground-state expectation values of any physical observable (see Methods for details). The phases described in the following correspond to extrapolations to the TDL. For that purpose, we study lattices of $N = 2L^2$ sites with periodic boundary conditions, and linear sizes up to $L = 18$.

To monitor the electronic properties of the system on increasing U, we extracted the single-particle excitation gap, $\Delta_{sp}(\mathbf{k})$, from the imaginary-time displaced Green's function (see Supplementary Information for details). This is the minimum energy necessary to extract one fermion from the system, and corresponds to the gap that can be observed in photoemission experiments. As shown in Fig. 1, $\Delta_{sp}(K) = 0$ for values of U/t below about 3.5, as expected for a semimetal. For larger values of U/t, the system enters an insulating phase as a result of interactions. The values of the gap are obtained by extrapolation of the QMC data to the TDL as shown in Fig. 2a.

From previous analysis of the model, long-range antiferromagnetic correlations are expected when the Mott insulator appears. We therefore measured the antiferromagnetic spin structure factor, S_{AF} (Supplementary Information), which indicates long-range antiferromagnetic order if $m_s^2 = \lim_{N\to\infty}(S_{AF}/N) > 0$. Figure 2b shows the QMC results together with a finite-size extrapolation. The results of this extrapolation are also presented in the phase diagram in Fig. 1. Antiferromagnetic order appears for $U/t > 4.3$, a value that is consistent with previous estimates for the onset of long-range antiferromagnetic order[26,27]. This leaves an extended window, $3.5 < U/t < 4.3$, within which the system is neither a semimetal nor an antiferromagnetic Mott insulator.

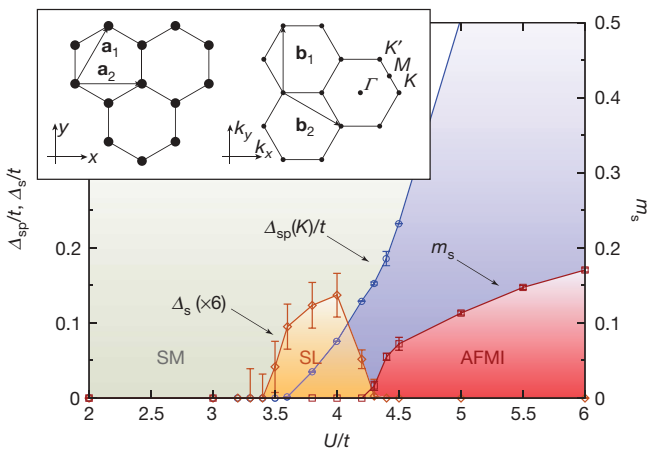

Figure 1 | Phase diagram for the Hubbard model on the honeycomb lattice at half-filling. The semimetal (SM) and the antiferromagnetic Mott insulator (AFMI) are separated by a gapped spin-liquid (SL) phase in an intermediate-coupling regime. $\Delta_{sp}(K)$ denotes the single-particle gap and Δ_s denotes the spin gap; m_s denotes the staggered magnetization, whose saturation value is 1/2. Error bars, s.e.m. Inset, the honeycomb lattice with primitive vectors $\mathbf{a}_1$ and $\mathbf{a}_2$, and the reciprocal lattice with primitive vectors $\mathbf{b}_1$ and $\mathbf{b}_2$. Open and filled sites respectively indicate two different sublattices. The Dirac points K and K' and the M and Γ points are marked.

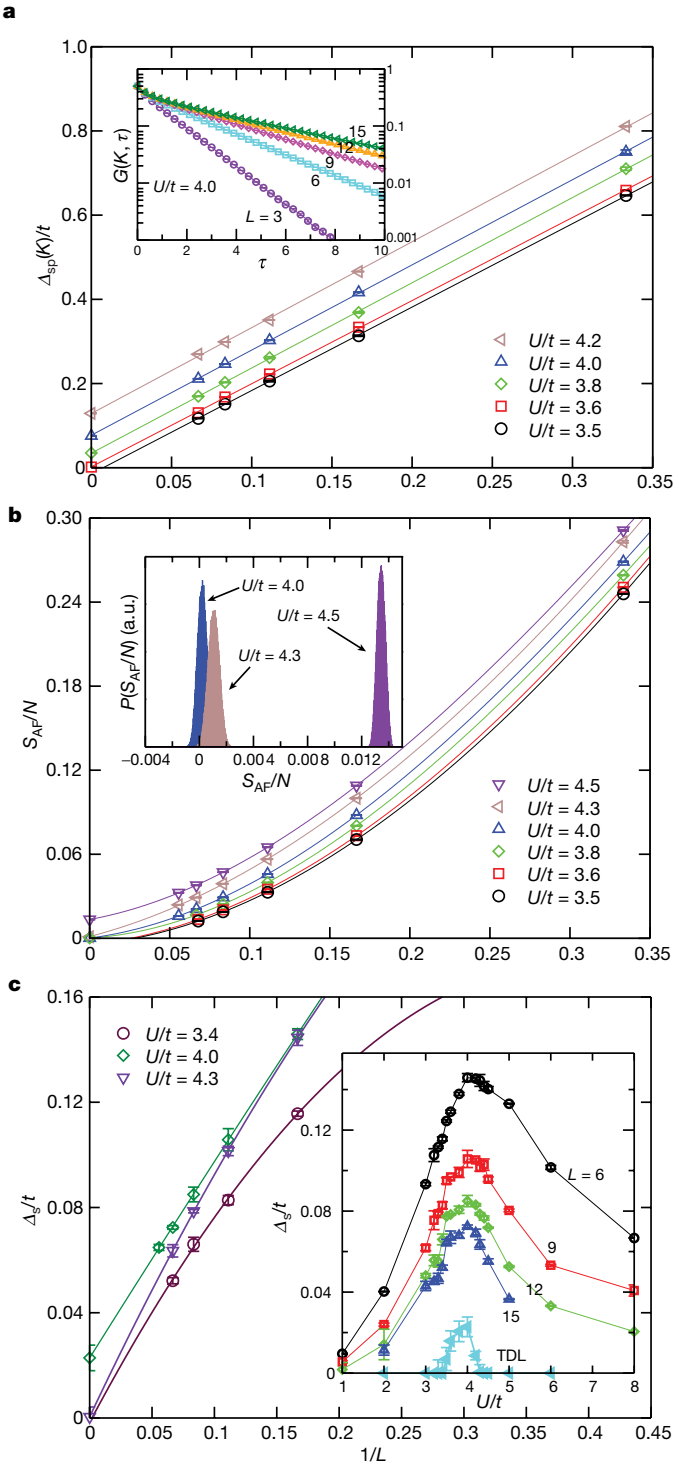

Figure 2 | Finite-size extrapolations of the excitation gaps and the antiferromagnetic structure factor. **a**, The single-particle gap at the Dirac point, $\Delta_{sp}(K)$, shown here for different values of U/t, is linear in $1/L$. $\Delta_{sp}(K)$ is obtained by fitting the tail of the Green's function, $G(K, \tau)$ (inset), to the form $e^{-\tau\Delta_{sp}(K)}$. **b**, Antiferromagnetic structure factor, S_{AF}, for various values of U/t, fitted using third-order polynomials in $1/L$. Antiferromagnetic order appears for $U/t > 4.3$, as seen in the histogram $P(S_{AF}/N)$ from a Monte Carlo bootstrapping analysis (inset). a.u., arbitrary units. **c**, Spin gap, Δ_s, for different values of U/t, fitted using second-order polynomials in $1/L$. Inset, Δ_s for $L = 6$, 9, 12 and 15, and the extrapolated values (TDL), as functions of U/t. Error bars, s.e.m.

Further details on the nature of this intermediate region are obtained by examining the spin excitation gap, which is extracted from the long-time behaviour of the imaginary-time displaced spin–spin

correlation function (Supplementary Information). We consider first the spin gap, Δ_s, in the staggered sector at $\mathbf{k} = \Gamma$, which vanishes in the antiferromagnetic phase owing to the emergence of two Goldstone modes, as well as in the gapless semimetal phase. Figure 2c shows finite-size estimates of Δ_s for different values of U/t, along with an extrapolation to the TDL. A finite value of Δ_s persists within the intermediate parameter regime, $3.5 < U/t < 4.3$, but Δ_s vanishes both within the semimetal phase and the antiferromagnetic phase. This 'dome' in the spin gap is also seen in the inset of Fig. 2c, which shows both the finite-size data and the extrapolated values of Δ_s as a function of U/t. We also calculated the uniform spin gap, Δ_u, by extrapolating to the TDL the spin gap observed at the lowest-magnitude finite $\mathbf{k}$ on each cluster. This gap is found to be even larger than Δ_s in the intermediate region (for example, $\Delta_u = 0.099 \pm 0.001$ (s.e.m.) for $U/t = 4$), and vanishes in the semimetal phase and the antiferromagnetic phase (Δ_u cannot be measured directly at $\mathbf{k} = \mathbf{0}$, because the uniform magnetization is a conserved quantity; see Supplementary Information). Hence, this intermediate insulating region corresponds to a spin-gap phase.

From analysing the U dependence of the kinetic energy density

$$E_{\mathrm{kin}} = \frac{1}{N}\left\langle -t \sum_{\langle i,j\rangle,\alpha} (c^{\dagger}_{i\alpha}c_{j\alpha} + c^{\dagger}_{j\alpha}c_{i\alpha}) \right\rangle$$

we obtain further insight into these different regimes and the emergence of local moments. As shown in Fig. 3, the curvature $\mathrm{d}^2E_{\mathrm{kin}}/\mathrm{d}U^2$ changes sign near $U/t = 4.3$. This marks a characteristic change from the weak-coupling region of positive curvature with delocalized electrons to the strong-coupling, antiferromagnetic region with negative curvature. In the second region, localized spins form and order in an antiferromagnetic state. In the intermediate spin-gap region, fluctuations are large enough to still prevent the formation of well-localized magnetic moments. We note that at around $U/t = 3.5$, a change in the curvature can be observed that adds to the established evidence for an intermediate phase.

Characterization of the spin-gap phase

The observation of a finite spin gap rules out a gapless spin liquid[12,13], quantum spin Hall states[14] and triplet superconductivity[16]. The remaining possibilities can be enumerated by considering the coupling to order parameters that lead to the opening of a mass gap in Dirac fermions[28] and hence account for the single-particle gap observed in the QMC data: the possibilities are singlet superconductivity, a quantum Hall state[29], charge-density-wave order[14] and a valence-bond crystal.

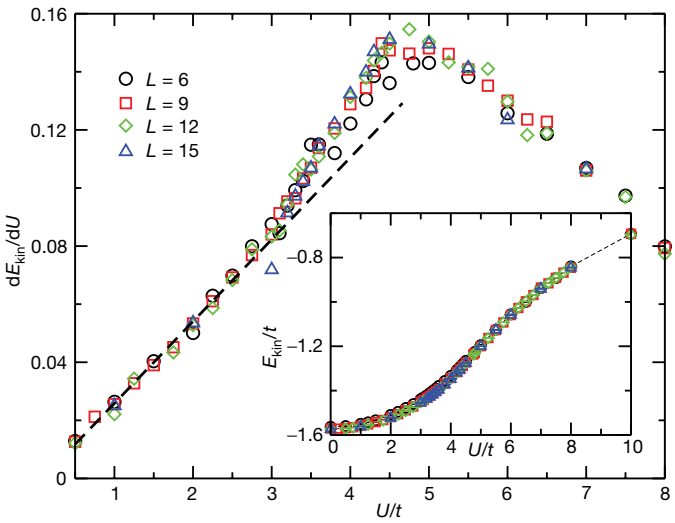

Figure 3 | Derivative $\mathrm{d}E_{\mathrm{kin}}/\mathrm{d}U$ of the kinetic energy density as a function of U/t for systems of different sizes. The dashed line is a fit to the low-U behaviour. The inset shows the QMC data for the kinetic energy density E_{kin} from which the derivative is obtained by numerical differentiation. Statistical errors (s.e.m.) are smaller than the symbol size.

To assess whether superconductivity arises in the vicinity of the Mott transition, we used the method of flux quantization, which probes the superfluid density and is hence independent of the specific symmetry of the pair wavefunction[30]. We let Φ be a magnetic flux traversing the centre of a torus on which the electronic system lies and denote by $E_0(\Phi/\Phi_0)$ the total ground-state energy, Φ_0 being the flux quantum. A superconducting state of Cooper pairs is present if in the TDL the macroscopic energy difference $E_0(\Phi/\Phi_0) - E_0(\Phi/\Phi_0 = 1/2)$ is a function with period 1/2 (ref. 31). In contrast, a metallic phase is characterized by $E_0(\Phi/\Phi_0) - E_0(\Phi/\Phi_0 = 1/2)$ vanishing as a power law as a function of system size, whereas in an insulating phase it would vanish exponentially. As shown in Supplementary Information, this quantity vanishes in the TDL both in the semimetallic state at $U = 0$ and at $U/t = 4$, that is, in the intermediate phase. In addition, we measured pair correlations, ruling out superconductivity in (extended) s-, p-, d-, and f-wave channels (Supplementary Information). Hence, both flux quantization as well as a direct measurement of pair correlations lead to no sign of superconductivity.

Both the charge density wave and the quantum Hall state trigger a breaking of the sublattice symmetry and thereby open a mass gap at the mean-field level. A detailed analysis of the charge–charge correlation functions rules out a charge density wave. Furthermore, we find no signature of (spin) currents in the ground state (Supplementary Information). This rules out the breaking of sublattice and time-reversal symmetries, which pertains to the quantum Hall state, in the pristine Hubbard model; it is possible that extensions of this model are necessary to reach such a state[14].

To examine the occurrence of a valence-bond crystal, we probed for dimer–dimer correlations between separated dimers formed by nearest-neighbour bonds (Supplementary Information). We find no valence-bond crystal either in the charge sector or in the spin sector. Figure 4 shows the results of this measurement in the spin sector, that is, the correlation between singlet dimers at $U/t = 4$. The striped bond is the one with respect to which correlations were determined. They are found to be short-ranged and consistent with the dominance of a RVB state within the hexagons of the honeycomb lattice. This can be seen by comparing the singlet correlations with those of an isolated hexagon (Fig. 4, inset), which is the classical example of the resonance phenomenon in conjugated π-electrons[32]. Accordingly, we find no long-range order from the dimer–dimer structure factors in Fourier space. Our results thus reveal a genuinely exotic state of matter, in which no spontaneous symmetry breaking is observed but a spin gap is present. It corresponds to a spin-liquid RVB state in the intermediate-coupling regime in the vicinity of the Mott transition.

Further insight into the RVB state

The QMC results presented above demonstrate the realization of a quantum spin-liquid state of correlated fermions on a non-frustrated, bipartite lattice. In principle, such quantum-disordered states can occur in different varieties; we thus aim to shed further light on the specific nature of the spin liquid described above. Gapless (algebraic) spin liquids and long-range RVB states are characterized by critical spin–spin correlations[9,33–36]. The observation of a finite spin gap excludes such candidate states while being consistent with the characterization of the observed spin liquid in terms of short-range RVB states[17,18,20–22], also in accordance with the observed short-range dimer–dimer correlations. Short-range RVB states are modelled in general using quantum dimer models[21–23], which capture the fluctuations of singlets in a RVB state, with dimers being a strong-coupling representation of nearest-neighbour singlets[21]. Depending on the lattice geometry, quantum dimer models can have a fully gapped short-range RVB phase, as, for example, on the triangular lattice[37], but also have spin-liquid states with gapless excitations, as is the case for bipartite lattices at the Rokhsar–Kivelson point[21] and within the U(1) spin-liquid

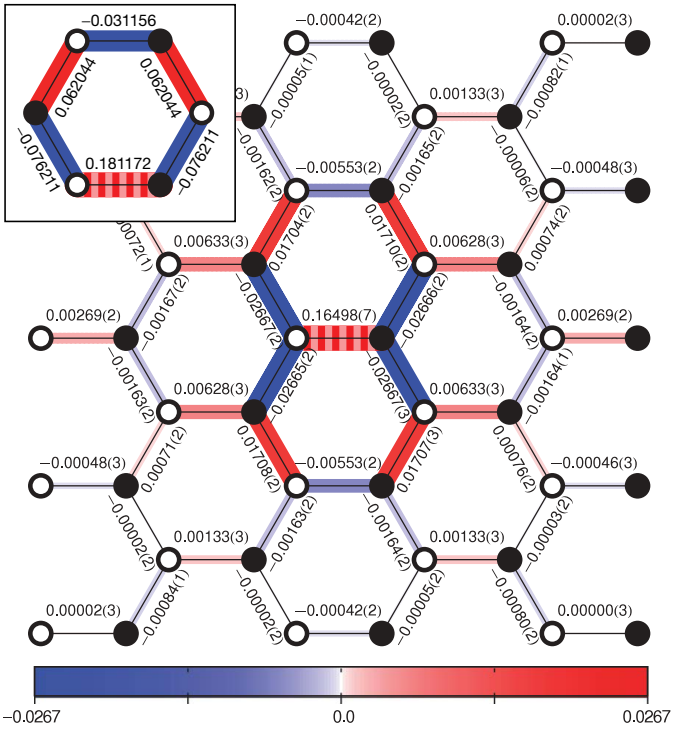

Figure 4 | Real-space plot of the spin dimer–dimer correlations. The correlation function $D_{ij,kl}$ (Supplementary Information) for a system with $L = 6$ at $U/t = 4$. Open and filled sites respectively indicate the different sublattices, as in Fig. 1. Inset, the same correlation for the isolated Hubbard hexagon, also at $U/t = 4$. The reference bonds are shown striped. Numbers in parentheses indicate the s.e.m. in the last digit.

phase stabilized for $d > 2$ spatial dimensions[38]. In the U(1) case, gapless singlet excitations constitute an emerging 'photon' soft mode. Fully gapped phases of quantum dimer models are furthermore characterized by having a non-trivial topological order, implying, for example, an emerging ground-state degeneracy of two-dimensional systems with periodic boundary conditions in the TDL[23,39].

To assess whether topological order can characterize the short-range RVB in our case, we examine the low-energy singlet excitations. As proven in an exact theorem[40], the finite systems used in our numerical simulations have a non-degenerate singlet ground state for any finite value of $U > 0$. Hence, degeneracy can only appear in the TDL. This implies that low-energy singlet states should be present, with excitation energies that decrease as the system size increases.

Because our QMC method projects out the finite system's ground state from a singlet trial wavefunction, we can monitor the expectation value of the internal energy, $E(\Theta)$, where Θ is the projection parameter (Methods). Here all contributions from singlet states that have the same quantum numbers as the ground state and that have a finite overlap with the trial wavefunction are included. For a given system of size N, we define Θ^* as the value of the projection parameter such that $(E(\Theta) - E_0)/N < \varepsilon$ for $\Theta > \Theta^*$, where E_0 is the ground-state energy and ε is an energy scale that we choose to satisfy $\varepsilon \ll (E_1 - E_0)/N$, E_1 being the energy of the first singlet excited state. Typically, we choose ε to be of the order of our statistical error in the energy density. Then $1/\Theta^*$ is a lower bound on the energy of the first singlet excited state (Supplementary Information).

Our analysis for various lattice sizes leads us to the conclusion that the singlet excitation gap stays above the spin gap in the TDL (Supplementary Information), providing no evidence for the emergence of a topological state. However, we cannot definitely exclude topological order if the relevant singlet states happen to have a vanishing overlap with our trial wavefunction. In future, it will be interesting to explore the low-energy singlets beyond the projective scheme and to probe for soft modes by a method similar, for example, to the construction of finite-momentum trial states in quantum dimer models[21,23]. Our findings, based on a controlled numerical framework, therefore open a new facet of quantum spin liquids, where an appreciable amount of doubly occupied sites are present, implying that the behaviour of the system extends well beyond the regime of localized spin physics.

Discussion and outlook

The presence of a spin liquid in the Hubbard model on the bipartite honeycomb lattice close to an antiferromagnetic Mott insulator resembles the situation in the organic antiferromagnet κ-(BEDT-TTF)$_2$Cu$_2$(CN)$_3$, which has been argued to have a spin-liquid state[41,42], although this system is on a triangular lattice and is hence frustrated. This difference can be reconciled starting from the strong-coupling limit of the Hubbard model, that is, a nearest-neighbour Heisenberg model, which close to the Mott transition acquires corrections that induce efficient frustrations to the spin degrees of freedom. In fact, a Klein Hamiltonian for a spin-liquid state on the honeycomb lattice, including extended exchange interactions, has been constructed[43]. A more pronounced difference is the appearance of superconductivity in the organic systems on the application of pressure, which is equivalent to the reduction of the ratio U/t in the Hubbard model[44]. The absence of superconductivity in our system could be due to the vanishing density of states at the Fermi energy. In this case, a finite coupling strength is needed, at least in the Bardeen–Cooper–Schrieffer frame[45]. However, having an unexpected realization of a short-range RVB state, it would be highly interesting to explore the consequences of doping, in a spirit close to the original proposition[19,20] for the copper oxides. In particular, for the fully gapped short-range RVB state, the finite spin gap sets the energy scale of pairing in the superconducting state[20]. In this respect, the value obtained for the spin gap is promising. The largest value attained is $\Delta_s \approx 0.025t$ (Fig. 1), which for $t = 1.5$–2.5 eV (in graphene $t = 2.8$ eV; ref. 6) corresponds to a temperature scale ranging from 400 to 700 K.

Although studies of doping are beyond the scope of our QMC approach owing to the sign problem, they could open interesting perspectives, for example in future experiments with ultracold atoms on a honeycomb optical lattice, or with honeycomb lattices based on group IV elements such as carbon (in the form of expanded graphene, to enhance the ratio U/t) or silicon (where the nearest-neighbour distance is expected to be approximately 50% larger than in graphene[24], such that correlations effects are enhanced). In fact, first attempts have succeeded in synthesizing single-crystal silicon monolayers[46].

METHODS SUMMARY

At half-filling, the finite-U region can be studied using the determinantal projective QMC algorithm to obtain ground-state expectation values of a physical observable by performing an imaginary-time evolution of a trial wavefunction that is required to be non-orthogonal to the ground state. The value Θ reached in the imaginary-time evolution corresponds to a projection parameter[47–49]. For a spin-singlet trial wavefunction, we found $\Theta = 40/t$ to be sufficient to obtain converged ground-state quantities within our statistical uncertainty. In the described simulations, we used a finite imaginary-time step, $\Delta\tau = 0.05/t$. By examining the limit in which $\Delta\tau \to 0$, we verified that this finite imaginary-time step produces no artefacts. Simulations were performed for systems of linear sizes $L = 3$, 6, 9, 12, 15 and 18 with $N = 2L^2$ sites. For periodic boundary conditions, these clusters all have nodal points K and hence allow a smooth extrapolation to the TDL. Quantities displaced in imaginary time were obtained using the approach in ref. 50.

Full Methods and any associated references are available in the online version of the paper at www.nature.com/nature.

Received 30 October 2009; accepted 17 February 2010.

1. Weinberg, S. *The Quantum Theory of Fields* Vol. 1 *Foundations* 1–48 (Cambridge Univ. Press, 2005).

2. Novoselov, K. *et al.* Two-dimensional gas of massless Dirac fermions in graphene. *Nature* **438,** 197–200 (2005).
3. Zhang, Y., Tan, Y.-W., Stormer, H. & Kim, P. Experimental observation of the quantum Hall effect and Berry's phase in graphene. *Nature* **438,** 201–204 (2005).
4. Zhang, H. *et al.* Topological insulators in Bi_2Se_3, Bi_2Te_3 and Sb_2Te_3 with a single Dirac cone on the surface. *Nature Phys.* **5,** 438–442 (2009).
5. Chen, Y. L. *et al.* Experimental realization of a three-dimensional topological insulator, Bi_2Te_3. *Science* **325,** 178–181 (2009).
6. Castro Neto, A. H., Guinea, F., Peres, N. M. R., Novoselov, K. S. & Geim, A. K. The electronic properties of graphene. *Rev. Mod. Phys.* **81,** 109–162 (2009).
7. Herbut, I. F. Interactions and phase transitions on graphene's honeycomb lattice. *Phys. Rev. Lett.* **97,** 146401 (2006).
8. Drut, J. E. & Lähde, T. A. Is graphene in vacuum an insulator? *Phys. Rev. Lett.* **102,** 026802 (2009).
9. Lee, P. A., Nagaosa, N. & Wen, X.-G. Doping a Mott insulator: physics of high-temperature superconductivity. *Rev. Mod. Phys.* **78,** 17–85 (2006).
10. Jördens, R., Strohmaier, N., Günter, K., Moritz, H. & Esslinger, T. A Mott insulator of fermionic atoms in an optical lattice. *Nature* **455,** 204–207 (2008).
11. Schneider, U. *et al.* Metallic and insulating phases of repulsively interacting fermions in a 3D optical lattice. *Science* **322,** 1520–1525 (2008).
12. Lee, S.-S. & Lee, P. A. U(1) gauge theory of the Hubbard model: spin liquid states and possible application to κ-(BEDT-TTF)$_2$Cu$_2$(CN)$_3$. *Phys. Rev. Lett.* **95,** 036403 (2005).
13. Hermele, M. SU(2) gauge theory of the Hubbard model and application to the honeycomb lattice. *Phys. Rev. B* **76,** 035125 (2007).
14. Raghu, S., Qi, X.-L., Honerkamp, C. & Zhang, S.-C. Topological Mott insulators. *Phys. Rev. Lett.* **100,** 156401 (2008).
15. Kane, C. L. & Mele, E. J. Quantum spin Hall effect in graphene. *Phys. Rev. Lett.* **95,** 226801 (2005).
16. Uchoa, B. & Castro Neto, A. H. Superconducting states of pure and doped graphene. *Phys. Rev. Lett.* **98,** 146801 (2007).
17. Anderson, P. W. Resonating valence bonds: a new kind of insulator? *Mater. Res. Bull.* **8,** 153–160 (1973).
18. Fazekas, P. & Anderson, P. W. On the ground state properties of the anisotropic triangular antiferromagnet. *Phil. Mag.* **30,** 423–440 (1974).
19. Anderson, P. W. The resonating valence bond state in La_2CuO_4 and superconductivity. *Science* **235,** 1196–1198 (1987).
20. Kivelson, S. A., Rokhsar, D. S. & Sethna, J. P. Topology of the resonating valence-bond state: solitons and high-T_c superconductivity. *Phys. Rev. B* **35,** 8865–8868 (1987).
21. Rokhsar, D. S. & Kivelson, S. A. Superconductivity and the quantum hard-core dimer gas. *Phys. Rev. Lett.* **61,** 2376–2379 (1988).
22. Moessner, R., Sondhi, S. L. & Fradkin, E. Short-ranged resonating valence bond physics, quantum dimer models, and Ising gauge theories. *Phys. Rev. B* **65,** 024504 (2001).
23. Moessner, R. & Raman, K. S. Quantum dimer models. Preprint at ⟨http://arxiv.org/abs/0809.3051⟩ (2008).
24. Cahangirov, S., Topsakal, M., Aktürk, E., Şahin, H. & Ciraci, S. Two- and one-dimensional honeycomb structures of silicon and germanium. *Phys. Rev. Lett.* **102,** 236804 (2009).
25. Duan, L.-M., Demler, E. & Lukin, M. Controlling spin exchange interactions of ultracold atoms in optical lattices. *Phys. Rev. Lett.* **91,** 090402 (2003).
26. Sorella, S. & Tosatti, E. Semi-metal-insulator transition of the Hubbard model in the honeycomb lattice. *Europhys. Lett.* **19,** 699–704 (1992).
27. Paiva, T., Scalettar, R. T., Zheng, W., Singh, R. R. P. & Otimaa, J. Ground-state and finite-temperature signatures of quantum phase transitions in the half-filled Hubbard model on a honeycomb lattice. *Phys. Rev. B* **72,** 085123 (2005).
28. Ryu, S., Mudry, C., Hou, C.-Y. & Chamon, C. Masses in graphene-like two-dimensional electronic systems: topological defects in order parameters and their fractional exchange statistics. *Phys. Rev. B* **80,** 205319 (2009).
29. Haldane, F. D. M. Model for a quantum Hall effect without Landau levels: condensed-matter realization of the "parity anomaly". *Phys. Rev. Lett.* **61,** 2015–2018 (1988).
30. Assaad, F. F., Hanke, W. & Scalapino, D. J. Flux quantization in the two-dimensional repulsive and attractive Hubbard models. *Phys. Rev. Lett.* **71,** 1915–1918 (1993).
31. Byers, N. & Yang, C. N. Theoretical considerations concerning quantized magnetic flux in superconducting cylinders. *Phys. Rev. Lett.* **7,** 46–49 (1961).
32. Pauling, L. *The Nature of the Chemical Bond* 183–220 (Cornell Univ. Press, 1960).
33. Rantner, W. & Wen, X. G. Spin correlations in the algebraic spin liquid: implications for high-T_c superconductors. *Phys. Rev. B* **66,** 144501 (2002).
34. Hermele, M. *et al.* On the stability of U(1) spin liquids in two dimensions. *Phys. Rev. B* **70,** 214437 (2004).
35. Assaad, F. F. Phase diagram of the half-filled two-dimensional SU(N) Hubbard-Heisenberg model: a quantum Monte Carlo study. *Phys. Rev. B* **71,** 075103 (2005).
36. Mizusaki, T. & Imada, M. Gapless quantum spin liquid, stripe, and antiferromagnetic phases in frustrated Hubbard models in two dimensions. *Phys. Rev. B* **74,** 014421 (2006).
37. Moessner, R. & Sondhi, S. L. Resonating valence bond phase in the triangular lattice quantum dimer model. *Phys. Rev. Lett.* **86,** 1881–1884 (2001).
38. Fradkin, E., Huse, D. A., Moessner, R., Oganesyan, V. & Sondhi, S. L. Bipartite Rokhsar-Kivelson points and Cantor deconfinement. *Phys. Rev. B* **69,** 224415 (2004).
39. Wen, X. G. Mean-field theory of spin-liquid states with finite energy gap and topological orders. *Phys. Rev. B* **44,** 2664–2672 (1991).
40. Lieb, E. H. Two theorems on the Hubbard model. *Phys. Rev. Lett.* **62,** 1201–1204 (1989).
41. Shimizu, Y., Miyagawa, K., Kanoda, K., Maesato, M. & Saito, G. Spin liquid state in an organic Mott insulator with a triangular lattice. *Phys. Rev. Lett.* **91,** 107001 (2003).
42. Yamashita, M. *et al.* Thermal-transport measurements in a quantum spin-liquid state of the frustrated triangular magnet κ-(BEDT-TTF)$_2$Cu$_2$(CN)$_3$. *Nature Phys.* **5,** 44–47 (2009).
43. Chayes, J. T., Chayes, L. & Kivelson, S. A. Valence bond ground states in a frustrated two-dimensional spin-1/2 Heisenberg antiferromagnet. *Commun. Math. Phys.* **123,** 53–83 (1989).
44. Nam, M.-S., Ardavan, A., Blundell, S. J. & Schlueter, J. A. Fluctuating superconductivity in organic molecular metals close to the Mott transition. *Nature* **449,** 584–587 (2007).
45. Kopnin, N. B. & Sonin, E. B. BCS superconductivity of Dirac electrons in graphene layers. *Phys. Rev. Lett.* **100,** 246808 (2008).
46. Nakano, H. *et al.* Soft synthesis of single-crystal silicon monolayer sheets. *Angew. Chem.* **118,** 6451–6454 (2006).
47. Sugiyama, G. & Koonin, S. E. Auxiliary field Monte-Carlo for quantum many-body ground states. *Ann. Phys.* **168,** 1–26 (1986).
48. Furukawa, N. & Imada, M. Optimization of initial state vector in the ground state algorithm of lattice fermion simulations. *J. Phys. Soc. Jpn* **60,** 3669–3674 (1991).
49. Assaad, F. F. & Evertz, H. G. *Computational Many-Particle Physics* 277–356 (Lect. Notes Phys. 739, Springer, 2008).
50. Feldbacher, M. & Assaad, F. F. Efficient calculation of imaginary-time-displaced correlation functions in the projector auxiliary-field quantum Monte Carlo algorithm. *Phys. Rev. B* **63,** 073105 (2001).

Supplementary Information is linked to the online version of the paper at www.nature.com/nature.

Acknowledgements We thank L. Balents, S. Capponi, A. H. Castro Neto, A. Georges, M. Hermele, A. Läuchli, E. Molinari, Y. Motome, S. Sachdev, K. P. Schmidt and S. Sorella for discussions. We are grateful to S. A. Kivelson for thoroughly reading our manuscript and providing important suggestions. F.F.A. is grateful to the Kavli Institute for Theoretical Physics of the University of California, Santa Barbara, for hospitality and acknowledges support by the Deutsche Forschungsgemeinschaft (DFG) through grants AS120/4-3 and FG1162. A.M. thanks the Aspen Center for Physics for hospitality and acknowledges partial support by the DFG through grant SFB/TRR21. S.W. acknowledges support by the DFG through grants SFB/TRR21 and WE3649. We thank the John von Neumann Institute for Computing, Jülich; the Hochleistungsrechenzentrum, Stuttgart; the BW Grid; and the Leibniz-Rechenzentrum, München, for the allocation of CPU time.

Author Contributions F.F.A. developed the simulation codes; Z.Y.M. and T.C.L. performed the simulations and analyses and prepared the figures; F.F.A., A.M. and S.W. directed the investigation and wrote the paper. The manuscript reflects the contributions of all authors.

Author Information Reprints and permissions information is available at www.nature.com/reprints. The authors declare no competing financial interests. Correspondence and requests for materials should be addressed to Z.Y.M. (meng@theo3.physik.uni-stuttgart.de).

METHODS

The projective QMC algorithm used for the simulations presented in this Article constitutes an unbiased, controlled and numerically exact method that is described in detail in refs. 47, 49. Within this scheme, ground-state expectation values of a physical observable A are obtained by performing an imaginary-time evolution:

$$\langle A\rangle = \lim_{\Theta\to\infty} \frac{\langle \Psi_T|e^{-\Theta H/2}Ae^{-\Theta H/2}|\Psi_T\rangle}{\langle \Psi_T|e^{-\Theta H}|\Psi_T\rangle}$$

Here we use the fact that the ground state of the Hubbard model on the honeycomb lattice is non-degenerate on any finite lattice at half-filling if there are equal numbers of sites in the two sublattices[40], and implicitly assume that the trial wavefunction, $|\Psi_T\rangle$, has a finite overlap with this ground state. The standard implementation of the algorithm requires the trial wavefunction to be a single Slater determinant.

The efficiency of the projective approach strongly depends on the choice of the trial wavefunction. To generate optimal trial wavefunctions, different approaches can be used. One possible strategy consists of optimizing the overlap of the trial wavefunction with the finite system's ground state[48]. An alternative is to specify a series of good quantum numbers that characterize the ground state. The trial wavefunction is then constructed so as to have these quantum numbers. We have chosen the second approach for our simulations, and generate the trial wavefunction from the non-interacting tight-binding model on a torus through which we apply a magnetic flux, Φ, corresponding to the vector potential $\mathbf{A} = \Phi\mathbf{a}_1/L$. In particular, we used a trial wavefunction of the form $|\Psi_T\rangle = |\Psi_T\rangle_\uparrow \otimes |\Psi_T\rangle_\downarrow$, where $|\Psi_T\rangle_\alpha$ denotes the ground state of the single-particle Hamiltonian in the spin-α (up or down) Hilbert subspace:

$$H^0_\alpha = -t\sum_{\langle j,k\rangle} c^\dagger_{j,\alpha}c_{k,\alpha}\exp\left(\frac{2\pi i}{\Phi_0}\int_j^k d\boldsymbol{\ell}\cdot\mathbf{A}\right) + \text{Hermitianconjugate}$$

Here $\Phi_0 = he/c$ denotes the flux quantum. At $\Phi = 0$ and for the considered finite lattices of linear size $L = 3n$ ($n \in \mathbb{N}$), the half-filled ground-state wavefunction of the above Hamiltonian is degenerate. Imposing an infinitesimal twist (we verified that taking $\Phi/\Phi_0 = 0.0001$ is sufficiently weak) lifts the twofold degeneracy of the single-particle states at the Dirac points K and K'. The so-produced filled-shell configuration guarantees the absence of a negative-sign problem and has total momentum $K + K' = \mathbf{G}$ ($\mathbf{G}$ being a reciprocal lattice vector) and zero total spin. We used this trial wavefunction for our zero-flux QMC simulations, and found an imaginary-time projection parameter of $\Theta = 40/t$ to be sufficient to obtain converged ground-state quantities within our statistical uncertainty.

For the presented simulations, we used an SU(2)-symmetric, discrete Hubbard–Stratonovich transformation that allows for a direct generalization of the simulation scheme to SU(N)-symmetric models[35]. In this approach, after performing the standard Trotter–Suzuki decomposition[49], the interaction part of the imaginary-time evolution operator is expressed as

$$e^{-\Delta\tau U(n_\uparrow+n_\downarrow-1)^2/2} = \sum_{l=\pm1,\pm2}\gamma(l)e^{i\sqrt{\Delta\tau U/2}\eta(l)(n_\uparrow+n_\downarrow-1)} + \mathcal{O}(\Delta\tau^4)$$

with the two functions γ and η of the four-valued auxiliary field $l = \pm1, \pm2$ taking the values

$$\gamma(\pm1) = 1+\sqrt{6}/3$$
$$\eta(\pm1) = \pm\sqrt{2(3-\sqrt{6})}$$
$$\gamma(\pm2) = 1-\sqrt{6}/3$$
$$\eta(\pm2) = \pm\sqrt{2(3+\sqrt{6})}$$

The advantage of this representation is the fact that for each Hubbard–Stratonovich configuration, the SU(2) spin symmetry of the Hubbard model is conserved explicitly. The above Hubbard–Stratonovich transformation produces an overall systematic error proportional to $\Delta\tau^3$ in the Monte Carlo estimate of observables; however, in comparison with the Trotter error, of order $\Delta\tau^2$, this is negligible. We used a finite imaginary-time step of $\Delta\tau = 0.05/t$ and verified, by examining the limit as $\Delta\tau \to 0$, that this value produces no artefacts. To extract the gaps associated with the various excitations of the system, in addition to equal-time correlations we calculated imaginary-time-displaced correlation functions. To calculate these imaginary-time-displaced quantities efficiently, we used an approach, introduced in ref. 50, which accounts for the fact that for a given auxiliary-field configuration the equal-time Green's function matrix is a projector.

Finally, we confirmed the validity of our implementation against exact diagonalization results on both $L = 2$ and $L = 3$ lattices.

SUPPLEMENTARY INFORMATION

In these supplementary sections, we provide further details about the simulation results mentioned in the main text. As a convenient notation, in the following $c^\dagger_{\mathbf{x}A\alpha}$ and $c^\dagger_{\mathbf{x}B\alpha}$ ($c_{\mathbf{x}A\alpha}$ and $c_{\mathbf{x}B\alpha}$) denote creation (annihilation) operators for fermions of spin $\alpha =\uparrow$ or $\downarrow$, on the lattice site that belongs to the sublattice A and B respectively, within the unit cell at position $\mathbf{x}$. Furthermore, $n_{\mathbf{x}a\alpha} = c^\dagger_{\mathbf{x}a\alpha}c_{\mathbf{x}a\alpha}$ and $n_{\mathbf{x}a} = \sum_\alpha n_{\mathbf{x}a\alpha}$ denote the local density operators, and $\mathbf{S}_{\mathbf{x}a} = \frac{1}{2}c^\dagger_{\mathbf{x}a\alpha}\boldsymbol{\sigma}_{\alpha\beta}c_{\mathbf{x}a\beta}$ the local spin operators, where $\boldsymbol{\sigma} = (\sigma_x, \sigma_y, \sigma_z)$ is the vector of Pauli matrices and $a \in \{A, B\}$. The corresponding operators in momentum space are obtained from

$$c_{\mathbf{k}a\alpha} = \frac{1}{L^2}\sum_{\mathbf{x}} e^{-i\mathbf{k}(\mathbf{x}+\mathbf{x}_a)}c_{\mathbf{x}a\alpha}, \tag{1}$$

where $\mathbf{x}_A = (0, 0)$ and $\mathbf{x}_B = (0, a)$, with a the distance between neighbouring lattice sites. Similarly, Fourier components $n_{\mathbf{k}a\alpha}$, $n_{\mathbf{k}a}$ and $\mathbf{S}_{\mathbf{k}a}$ of the density and spin operators are defined. For the following, it is also convenient to introduce the three lattice vectors related to the three nearest neighbour bonds,

$$\boldsymbol{\delta}_1 = (0, 0), \quad \boldsymbol{\delta}_2 = -\mathbf{a}_2, \quad \boldsymbol{\delta}_3 = \mathbf{a}_1 - \mathbf{a}_2,$$

where $\mathbf{a}_1$ and $\mathbf{a}_2$ are shown in Fig. 1, as well as

$$\mathbf{r}_1 = \mathbf{a}_2, \quad \mathbf{r}_2 = \mathbf{a}_2 - \mathbf{a}_1, \quad \mathbf{r}_3 = -\mathbf{a}_1, \quad \mathbf{r}_4 = -\mathbf{r}_1, \quad \mathbf{r}_5 = -\mathbf{r}_2, \quad \mathbf{r}_6 = -\mathbf{r}_3$$

connecting a given lattice site to its six next-nearest neighouring lattice sites. For the correlation between two local operators O_1 and O_2, we employ a short notation for the cummulant,

$$\langle\langle O_1 O_2\rangle\rangle := \langle O_1 O_2\rangle - \langle O_1\rangle\langle O_2\rangle. \tag{2}$$

Most of the following results concern the intermediate spin liquid phase, and we present in those cases quantum Monte Carlo data for the representative value of $U/t = 4$.

1 Green's function and single-particle gap

To probe the single-particle properties, we measured the imaginary-time displaced Green's function

$$G(\mathbf{k}, \tau) = \frac{1}{2}\sum_a \langle c^\dagger_{\mathbf{k}a\uparrow}(\tau)c_{\mathbf{k}a\uparrow}(0)\rangle = \frac{1}{2}\sum_a \langle c^\dagger_{\mathbf{k}a\downarrow}(\tau)c_{\mathbf{k}a\downarrow}(0)\rangle, \tag{3}$$

where $c^{(\dagger)}_{\mathbf{k}a\alpha}(\tau) = e^{\tau H} c^{(\dagger)}_{\mathbf{k}a\alpha} e^{-\tau H}$. The single-particle gap $\Delta_{sp}(\mathbf{k})$ is obtained from $G(\mathbf{k},\tau) \propto \exp(-\tau\Delta_{sp}(\mathbf{k}))$ at large imaginary time τ, and corresponds to the particle (or hole) excitation energy with respect to the chemical potential $\mu = 0$ at half-filling in this particle-hole symmetric system. At $U = 0$, the single-particle gap vanishes at the Dirac points K and K' (cf. Fig. 1 for our notation in momentum space), and we thus considered $\Delta_{sp}(K)$ in detail. The quantum Monte Carlo data for $G(K,\tau)$ and $\Delta_{sp}(K)$ is presented in the main text.

2 Spin correlations and S_{AF}

The antiferromagnetic order at large values of U/t resides within the unit cell of the honeycomb lattice. Hence, the spin structure factor for antiferromagnetic order relates to the staggered spin correlations at the Γ point (cf. Fig. 1 for our notation in momentum space),

$$S_{AF} = \langle [\sum_{\mathbf{x}} (\mathbf{S}_{\mathbf{x}A} - \mathbf{S}_{\mathbf{x}B})]^2 / N \rangle. \tag{4}$$

In addition to the above structure factor, we also probed directly the spin-spin correlation functions

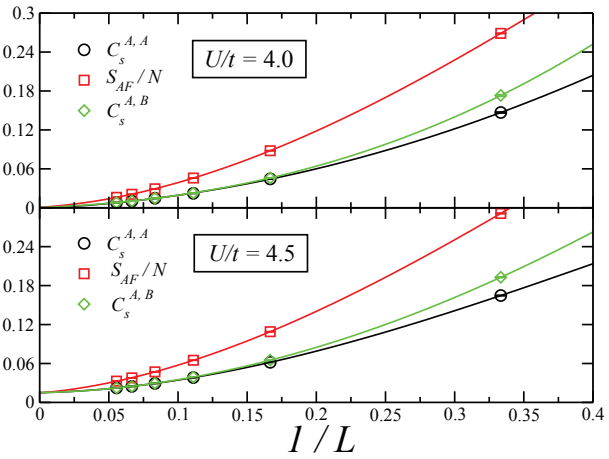

Supplementary Figure 1 | Comparison of the finite size scaling between the spin correlations $C_s^{A,A}$ and $C_s^{A,B}$ at the largest available distance and the staggered structure factor S_{AF} at $U/t = 4$ (upper panel) and $U/t = 4.5$ (lower panel), using 3rd order polynomials in $1/L$. Error bars denote standard errors.

$$C_s^{a,b}(\mathbf{x},\mathbf{y}) = \langle\langle \mathbf{S}_{\mathbf{x}a} \cdot \mathbf{S}_{\mathbf{y}b} \rangle\rangle \tag{5}$$

at the largest available distance $\mathbf{d}_L = ([L/2+1]-1)\,\mathbf{a}_1 + ([L/2+1]-1)\,\mathbf{a}_2$ for different system sizes, and performed a finite size scaling of both $C_s^{A,A} = C_s^{A,A}(0,\mathbf{d}_L)$ and $C_s^{A,B} = -C_s^{A,B}(0,\mathbf{d}_L)$.

A comparison of the scaling of these quantities to S_{AF} is shown for both $U/t = 4$ and $U/t = 4.5$ in Suppl. Fig. 1, exhibiting the consistency between these different approaches to quantify the spin correlations in the ground state.

3 Spin excitation gaps

The gaps for spin excitations at momentum vector $\mathbf{k}$ are obtained from the imaginary-time displaced spin-spin correlation functions for both the staggered sector,

$$S_s(\mathbf{k},\tau) = \langle\langle(\mathbf{S}_{\mathbf{k}A}(\tau) - \mathbf{S}_{\mathbf{k}B}(\tau)) \cdot (\mathbf{S}_{\mathbf{k}A}(0) - \mathbf{S}_{\mathbf{k}B}(0))\rangle\rangle, \quad (6)$$

as well as the uniform sector,

$$S_u(\mathbf{k},\tau) = \langle\langle(\mathbf{S}_{\mathbf{k}A}(\tau) + \mathbf{S}_{\mathbf{k}B}(\tau)) \cdot (\mathbf{S}_{\mathbf{k}A}(0) + \mathbf{S}_{\mathbf{k}B}(0))\rangle\rangle, \quad (7)$$

where $\mathbf{S}_{\mathbf{k},a}(\tau) = e^{\tau H}\mathbf{S}_{\mathbf{k},a}e^{-\tau H}$. Similarly as for the single-particle gap, the spin excitation gaps are obtained from $S_s(\mathbf{k},\tau) \propto \exp(-\tau\Delta_s(\mathbf{k}))$, and $S_u(\mathbf{k},\tau) \propto \exp(-\tau\Delta_u(\mathbf{k}))$ at large imaginary time τ. The staggered spin gap $\Delta_s = \Delta_s(\Gamma)$ can be calculated directly via the staggered spin-spin

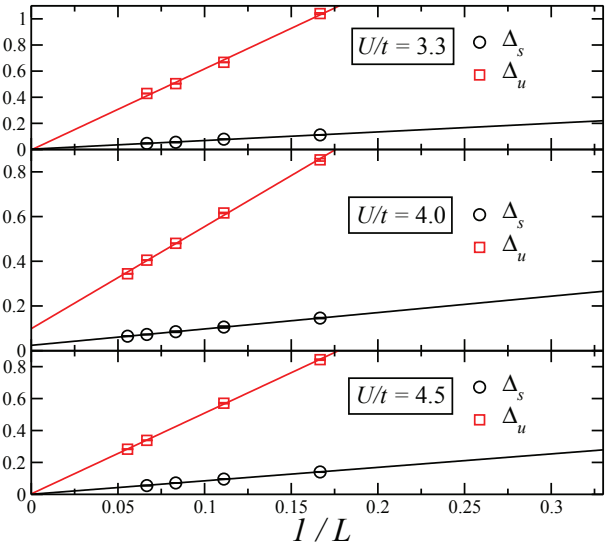

Supplementary Figure 2 | Comparison of the finite size scaling between the staggered spin gap Δ_s and the uniform spin gap Δ_u at $U/t = 3.3, 4$ and 4.5 (top to bottom). The extrapolated values in the thermodynamic limit for $U/t = 4$ are $\Delta_s = 0.023 \pm 0.007$ (s.e.m.) and $\Delta_u = 0.099 \pm 0.001$ (s.e.m.). Error bars denote standard errors.

correlations at the Γ point. However, since the total magnetization $\mathbf{S}_{tot} = \mathbf{S}_{\Gamma A} + \mathbf{S}_{\Gamma B}$ commutes

with the Hamiltonian of the system, $[\mathbf{S}_{tot}, H] = 0$, the uniform spin gap Δ_u cannot be extracted from the uniform spin-spin correlations at the Γ point in a canonical quantum Monte Carlo simulation. Instead, one obtains $\Delta_u = \lim_{\mathbf{k}\to\Gamma} \Delta_u(\mathbf{k})$ from measurements performed at the finite momenta closest to the Γ point for each finite system. Supplementary Fig. 2 shows the finite size data for these gaps at $U/t = 3.3, 4$ and 4.5. For $U/t = 4$, both gaps scale to finite values in the thermodynamic limit, with Δ_u being about four times as large as Δ_s. For the other two values of U/t, both gaps clearly vanish in the thermodynamic limit.

4 Density correlations

The density-density correlation function is given by

$$C_d^{a,b}(\mathbf{x}, \mathbf{y}) = \langle\langle n_{\mathbf{x}a} n_{\mathbf{y}b}\rangle\rangle, \tag{8}$$

where $a, b \in \{A, B\}$. At half-filling, $\langle n_{\mathbf{x}a}\rangle = \langle n_{\mathbf{x}b}\rangle = 1$. Supplementary Fig. 3 shows the finite size scaling of the density correlations at the largest distance, $C_d^{A,A} = |C_d^{A,A}(0, \mathbf{d}_L)|$ and $C_d^{A,B} = |C_d^{A,B}(0, \mathbf{d}_L)|$ at $U/t = 4$. Both scale to zero in the thermodynamic limit, and no long-range density correlations persist. Furthermore, in comparison with the spin correlations, the density correlations are seen to be significantly weaker and essentially zero within the statistical error for system sizes $L \geq 9$. Consistently, we also find no long-range density ordering when analyzing the density structure factor (not shown).

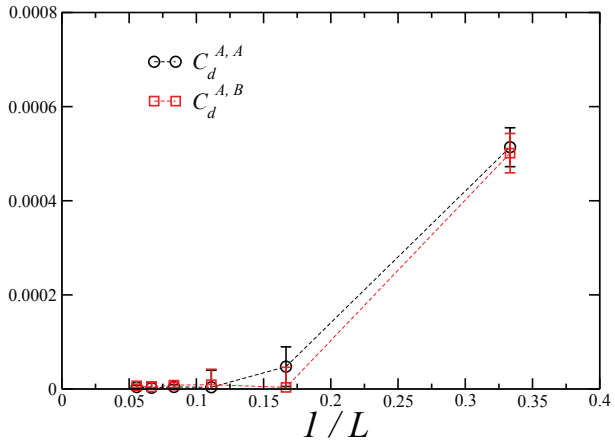

Supplementary Figure 3 | Finite size scaling of the density correlation functions $C_d^{A,A}$ and $C_d^{A,B}$ at $U/t = 4$. Error bars denote standard errors.

5 Dimer-dimer correlations - charge sector

In this section, we present our results on the dimer-dimer correlations in the charge sector. We measured both the correlations between the kinetic energy bond operators and the current operators. The spin sector is treated in the following section.

Correlations between the kinetic energy bond operators

$$k(\mathbf{x}, a; \mathbf{y}, b) = \sum_{\alpha} (c^{\dagger}_{\mathbf{x}a\alpha} c_{\mathbf{y}b\alpha} + c^{\dagger}_{\mathbf{y}b\alpha} c_{\mathbf{x}a\alpha}), \tag{9}$$

and the current operators

$$j(\mathbf{x}, a; \mathbf{y}, b) = -i \sum_{\alpha} (c^{\dagger}_{\mathbf{x}a\alpha} c_{\mathbf{y}b\alpha} - c^{\dagger}_{\mathbf{y}b\alpha} c_{\mathbf{x}a\alpha}) \tag{10}$$

can be defined between both nearest-neighbour and next-nearest neighbour sites on the honeycomb lattice.

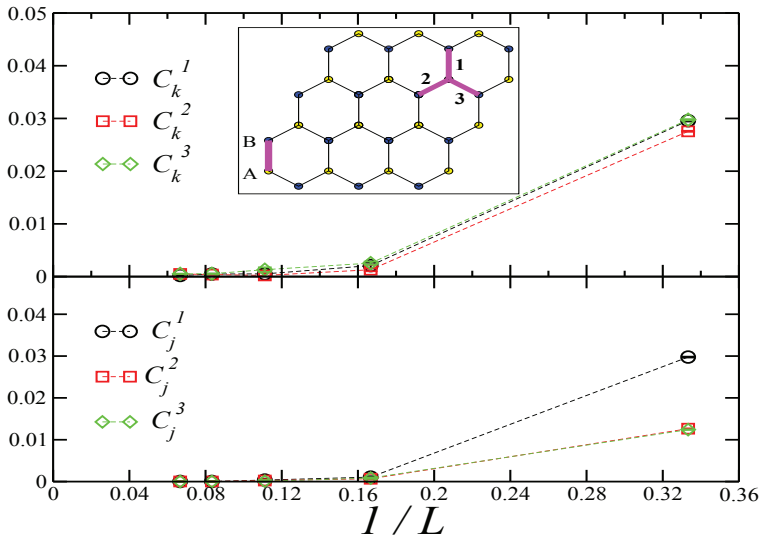

Supplementary Figure 4 | Finite size scaling of the nearest-neighbour correlations C_k^i and C_j^i at $U/t = 4$. The inset illustrates the three inequivalent directions with respect to the reference bond marked by AB. Error bars denote standard errors.

To probe for VBC order in the kinetic energy sector, we measured the three inequivalent dimer-dimer correlation functions

$$C_k^i = |\langle\langle k(0, A; 0, B) k(\mathbf{d}_L, A; \mathbf{d}_L + \boldsymbol{\delta}_i, B)\rangle\rangle|, \quad i = 1, 2, 3, \tag{11}$$

at the largest distance $\mathbf{d}_L$ on the finite lattices. For an illustration of the different relative bond orientations, see the inset of Suppl. Fig. 4. The upper panel of Suppl. Fig. 4 shows the finite size scaling of the C_k^i at $U/t = 4$. These correlations scale to zero in the thermodynamic limit, hence no long-ranged bond order in the kinetic energy persists. Furthermore, in comparison with the spin correlations, these correlations are also seen to be significantly weaker.

To probe for the persistence of nearest-neighbour currents in the ground state, we measured the current-current correlation functions between the bonds of the honeycomb lattice

$$C_j^i = |\langle\langle j(0, A; 0, B) j(\mathbf{d}_L, A; \mathbf{d}_L + \boldsymbol{\delta}_i, B)\rangle\rangle|, \quad i = 1, 2, 3, \tag{12}$$

at the largest distance $\mathbf{d}_L$ on the finite lattices. The corresponding finite size scalings are shown in the lower panel of Suppl. Fig. 4. Again, long range correlations in the thermodynamic limit can be clearly excluded, indicating the absence of currents between nearest neighbour sites in the ground state.

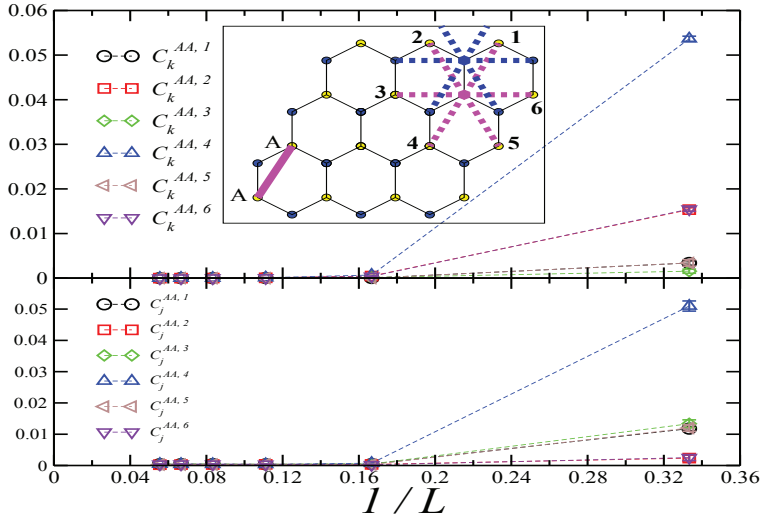

Supplementary Figure 5 | Finite size scaling of the next-nearest neighbour correlations $C_k^{AA,i}$ and $C_j^{AA,i}$ at the largest distance at $U/t = 4$. The inset illustrates the inequivalent directions with respect to the reference bond marked by AA, with the lower (upper) star corresponding to equal (different) sublattices. Error bars denote standard errors.

To probe for bond order and currents between next-nearest neighbour sites, we measured all inequivalent next-nearest neighbour bond-bond and current-current correlation functions at the

largest distances both within the same sublattice and between the two sublattices,

$$C_k^{AA,i} = |\langle\langle k(0,A;\mathbf{r}_1,A)k(\mathbf{d}_L,A;\mathbf{d}_L+\mathbf{r}_i,A)\rangle\rangle|, \quad (13)$$
$$C_j^{AA,i} = |\langle\langle j(0,A;\mathbf{r}_1,A)j(\mathbf{d}_L,A;\mathbf{d}_L+\mathbf{r}_i,A)\rangle\rangle|, \quad (14)$$
$$C_k^{AB,i} = |\langle\langle k(0,A;\mathbf{r}_1,A)k(\mathbf{d}_L,B;\mathbf{d}_L+\mathbf{r}_i,B)\rangle\rangle|, \quad (15)$$
$$C_j^{AB,i} = |\langle\langle j(0,A;\mathbf{r}_1,A)j(\mathbf{d}_L,B;\mathbf{d}_L+\mathbf{r}_i,B)\rangle\rangle|, \quad i=1,...,6. \quad (16)$$

For an illustration of the different relative bond orientations, see the inset of Suppl. Fig. 5. The quantum Monte Carlo data for the correlations within the same sublattice at $U/t = 4$ are shown in Suppl. Fig. 5. Both $C_k^{AA,i}$ and $C_j^{AA,i}$ all scale to zero in the thermodynamic limit. The corresponding correlations between the two sublattices similarly decay to zero in the thermodynamic limit (not shown). Thus no bond ordering nor currents persist between next-nearest neighbour sites in the ground state at $U/t = 4$.

6 Dimer-dimer correlations - spin sector

In the spin sector, we measured the dimer-dimer correlation functions

$$D_{ij,kl} = \langle\langle(\mathbf{S}_i\cdot\mathbf{S}_j - \frac{1}{4})(\mathbf{S}_k\cdot\mathbf{S}_l - \frac{1}{4})\rangle\rangle \quad (17)$$

where ij and kl are each nearest neighbour sites on the honeycomb lattice. The quantum Monte Carlo results for these correlations are shown and discussed in the main text.

We furthermore measured correlations between the spin-current operators

$$j_s(\mathbf{x},a;\mathbf{y},b) = -i\sum_\alpha(-1)^\alpha(c^\dagger_{\mathbf{x}a\alpha}c_{\mathbf{y}b\alpha} - c^\dagger_{\mathbf{y}b\alpha}c_{\mathbf{x}a\alpha}) \quad (18)$$

as well as the spin-bond operators

$$k_s(\mathbf{x},a;\mathbf{y},b) = \sum_\alpha(-1)^\alpha(c^\dagger_{\mathbf{x}a\alpha}c_{\mathbf{y}b\alpha} + c^\dagger_{\mathbf{y}b\alpha}c_{\mathbf{x}a\alpha}), \quad (19)$$

for next-nearest neighbour sites. We measured these correlations between all inequivalent pairs of next-nearest neighbour sites both within the same sublattice and between the two sublattices at the largest distance on the finite lattices,

$$C_{s-k}^{AA,i} = |\langle\langle k_s(0,A;\mathbf{r}_1,A)k_s(\mathbf{d}_L,A;\mathbf{d}_L+\mathbf{r}_i,A)\rangle\rangle|, \quad (20)$$
$$C_{s-j}^{AA,i} = |\langle\langle j_s(0,A;\mathbf{r}_1,A)j_s(\mathbf{d}_L,A;\mathbf{d}_L+\mathbf{r}_i,A)\rangle\rangle|, \quad (21)$$
$$C_{s-k}^{AB,i} = |\langle\langle k_s(0,A;\mathbf{r}_1,A)k_s(\mathbf{d}_L,B;\mathbf{d}_L+\mathbf{r}_i,B)\rangle\rangle|, \quad (22)$$
$$C_{s-j}^{AB,i} = |\langle\langle j_s(0,A;\mathbf{r}_1,A)j_s(\mathbf{d}_L,B;\mathbf{d}_L+\mathbf{r}_i,B)\rangle\rangle|, \quad i=1,..,6. \quad (23)$$

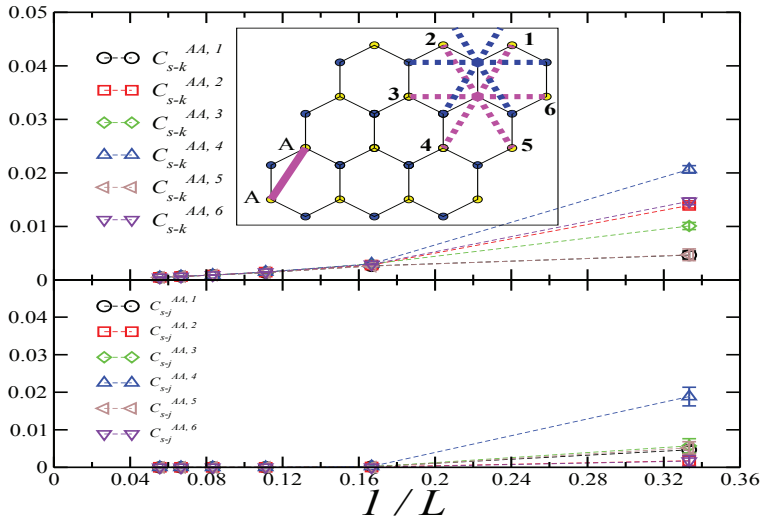

Supplementary Figure 6 | Finite size scaling of the next-nearest neighbour correlations $C_{s-k}^{AA,i}$ and $C_{s-j}^{AA,i}$ at the largest distance at $U/t = 4$. The inset illustrates the inequivalent directions with respect to the reference bond marked by AA, with the lower (upper) star corresponding to equal (different) sublattices. Error bars denote standard errors.

For an illustration of the different relative bond orientations, see the inset of Suppl. Fig. 6. Supplementary Fig. 6 shows the finite size scaling of the correlations within the same sublattice at $U/t = 4$. They all decay to zero in the thermodynamic limit. The corresponding correlations between different sublattices show a similar behavior (not shown). Thus no spin-bond order nor spin-currents persist between next-nearest neighbour sites in the ground state at $U/t = 4$.

7 Flux quantization measurement for superconductivity

In the flux quantization measurement, we thread a magnetic flux Φ, in units of the flux quantum Φ_0, through the centre of a torus on which the electronic system lies. From the functional form of the ground state energy with respect to the threaded flux, $E_0(\Phi/\Phi_0)$, we can distinguish between normal and superconducting ground states. The signature of the latter requires that the macroscopic energy difference $E_0(\Phi/\Phi_0) - E_0(\Phi/\Phi_0 = 1/2)$ scales in the thermodynamic limit to a periodic function of period $1/2$, and the occurrence of an energy barrier between $\Phi/\Phi_0 = 0$ and $\Phi/\Phi_0 = 1/2$. In contrast, a metallic phase is characterized by $E_0(\Phi/\Phi_0) - E_0(\Phi/\Phi_0 = 1/2)$ vanishing as a power law as a function of system size, while in an insulating phase, it would vanish exponentially. Figure 7 compares the QMC results of the macroscopic energy difference at $U = 0$ with that at $U/t = 4$. In both cases one clearly observes the vanishing of this quantity in the ther-

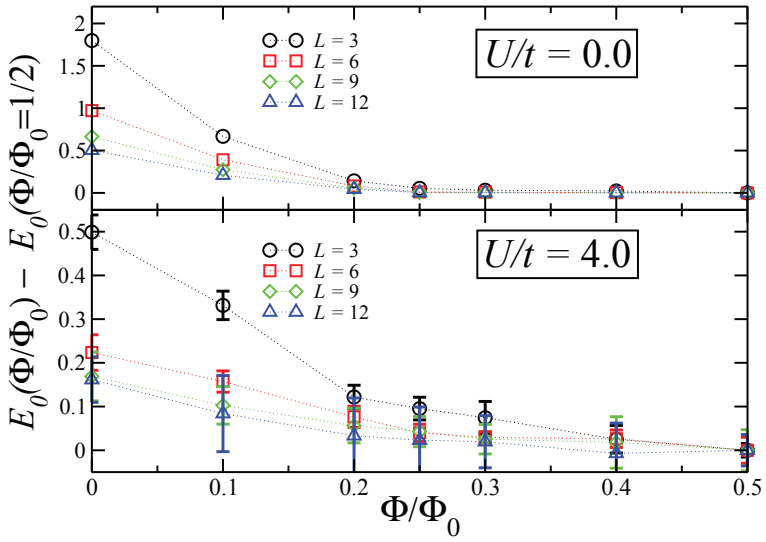

Supplementary Figure 7 | The energy difference of $E_0(\Phi/\Phi_0) - E(\Phi/\Phi_0 = 1/2)$ for different system sizes at $U/t = 0$ and $U/t = 4$. Note that the scale for $U/t = 4$ is four times smaller than for $U/t = 0$. The flattening of the energy differences exclude the superconducting ground state at both $U/t = 0$ and $U/t = 4$. Error bars denote standard errors.

modynamic limit. Hence, no signal for superconductivity is obtained from these flux quantization measurements.

8 Order parameters for superconductivity

Order parameters for superconductivity are in principle obtained from considering the irreducible representations of the D_6 point group of the honeycomb lattice, which can be described as a triangular lattice with a basis of two atoms in the sublattices A and B, respectively. The Cooper pair wave function of a superconducting state is a product of a spin, orbital and a sublattice component. Since Pauli's principle requires the wave function to be antisymmetric under particle exchange, we obtain the following possibilities for spin-singlet pairing: for an even (odd) orbital part, the wave function must be symmetric (antisymmetric) under sublattice exchange. It is convenient to introduce pair creation operators in the singlet channel

$$\Delta^\dagger(\mathbf{x}, a; \mathbf{y}, b) = c^\dagger_{\mathbf{x}a\uparrow} c^\dagger_{\mathbf{y}b\downarrow} - c^\dagger_{\mathbf{x}a\downarrow} c^\dagger_{\mathbf{y}b\uparrow}, \tag{24}$$

where $a, b \in \{A, B\}$. The operator

$$\Delta^\dagger_s(\mathbf{x}) = \frac{1}{2}(\Delta^\dagger(\mathbf{x}, A; \mathbf{x}, A) + \Delta^\dagger(\mathbf{x}, B; \mathbf{x}, B)) \tag{25}$$

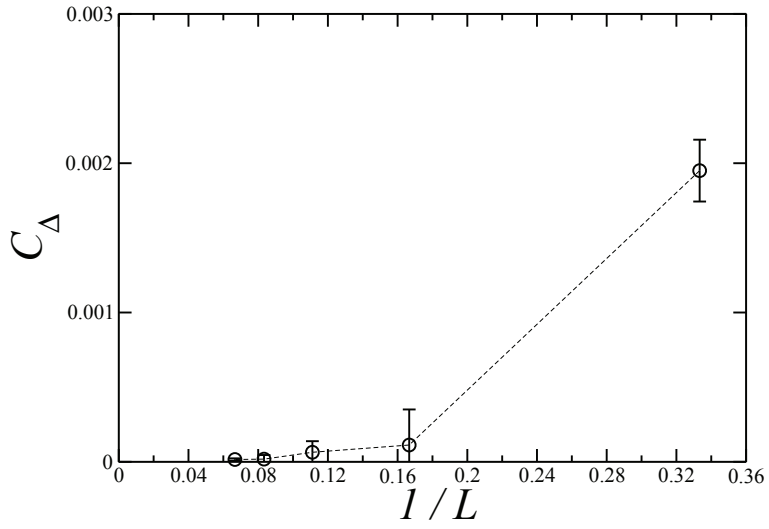

Supplementary Figure 8 | Finite size scaling of on-site s-wave pairing correlation C_Δ at $U/t = 4$.

describes on-site s-wave pairing, which is symmetric under sublattice exchange. In Suppl. Fig. 8, we show the s-wave pair-pair correlation function $C_\Delta = |\langle \Delta_s(0)\Delta_s^\dagger(\mathbf{d}_L)\rangle|$ at the largest distance at $U/t = 4$. No long-ranged pairing correlation sustains to the thermodynamic limit; instead, the on-site pair-pair correlation function decreases rapidly.

Extended pair creation operators based on nearest neighbour pairing can be expressed in terms of phase factors $f_1^a, f_2^a, f_3^a, a \in \{A, B\}$,

$$\Delta^\dagger(\mathbf{x}, f_1^A, f_2^A, f_3^A, f_1^B, f_2^B, f_3^B) = \sum_{i=1}^{3}[f_i^A \Delta^\dagger(\mathbf{x}, A; \mathbf{x} + \boldsymbol{\delta}_i, B) + f_i^B \Delta^\dagger(\mathbf{x}, B; \mathbf{x} - \boldsymbol{\delta}_i, A)] \quad (26)$$

For an extended s-wave,

$$\Delta_{ext.-s}^\dagger(\mathbf{x}) = \Delta^\dagger(\mathbf{x}, 1, 1, 1, 1, 1, 1). \quad (27)$$

Nearest neighbour p-wave states relate to

$$\Delta_{p_x}^\dagger(\mathbf{x}) = \Delta^\dagger(\mathbf{x}, 0, +1, -1, 0, -1, +1), \quad (28)$$
$$\Delta_{p_y}^\dagger(\mathbf{x}) = \Delta^\dagger(\mathbf{x}, 0, +1, +1, 0, -1, -1), \quad (29)$$

and nearest neighbour d-wave states to

$$\Delta_{d_{xy}}^\dagger(\mathbf{x}) = \Delta^\dagger(\mathbf{x}, 0, +1, -1, 0, +1, -1), \quad (30)$$
$$\Delta_{d_{x^2-y^2}}^\dagger(\mathbf{x}) = \Delta^\dagger(\mathbf{x}, -2, +1, +1, -2, +1, +1). \quad (31)$$

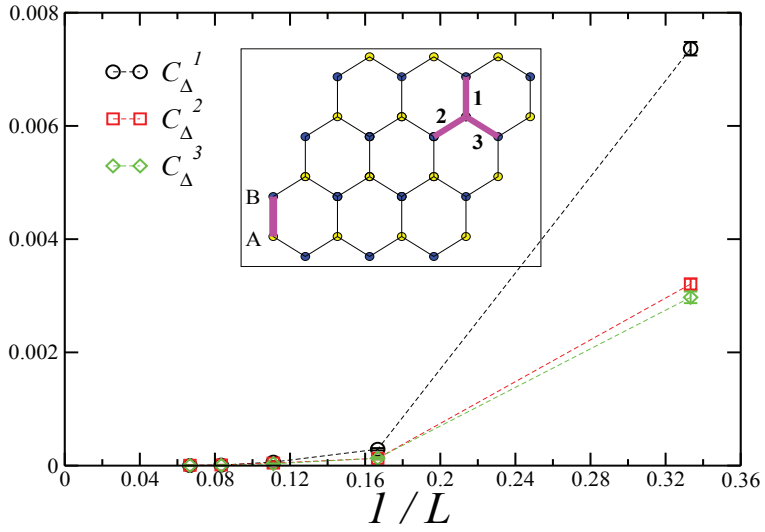

Supplementary Figure 9 | Finite size scaling of nearest neigbour pair correlation C^i_Δ at $U/t = 4$. The inset illustrates the three inequivalent directions with respect to the reference bond marked by AB. Error bars denote standard errors.

In terms of next-nearest neighbours, one furthermore obtains the singlet f-wave state

$$\Delta^\dagger_f(\mathbf{x}) = \sum_{j=i}^{6}(-1)^i[\Delta^\dagger(\mathbf{x}, A; \mathbf{x}+\mathbf{r}_i, A) - \Delta^\dagger(\mathbf{x}, B; \mathbf{x}+\mathbf{r}_i, B)]. \tag{32}$$

In order to probe for superconductivity based on nearest neighbour or next-nearest neighbour pairing in the above symmetry sectors, we directly measured in real-space the various inequivalent pair-pair correlation functions at the largest distances on the finite lattices, i.e.

$$C^i_\Delta = |\langle\langle\Delta(0, A; 0, B)\Delta^\dagger(\mathbf{d}_L, A; \mathbf{d}_L + \boldsymbol{\delta}_i, B)\rangle\rangle|, \quad i = 1, 2, 3, \tag{33}$$

for the nearest neighbour pairing states, and

$$C^{AA,i}_\Delta = |\langle\langle\Delta(0, A; \mathbf{r}_1, A)\Delta^\dagger(\mathbf{d}_L, A; \mathbf{d}_L + \mathbf{r}_i, A)\rangle\rangle| \tag{34}$$

$$C^{AB,i}_\Delta = |\langle\langle\Delta(0, A; \mathbf{r}_1, A)\Delta^\dagger(\mathbf{d}_L, B; \mathbf{d}_L + \mathbf{r}_i, B)\rangle\rangle|, \quad i = 1, ..., 6, \tag{35}$$

for next-nearest neighbour pairing states both within the same sublattice and between the two sublattices. As shown in Suppl. Fig. 9 and Suppl. Fig. 10, both nearest neighbour and next-nearest neighbour pair-pair correlation functions are very weak, even reaching zero within statistical errors for $L \geq 9$. From this, we exclude pairing in all the above symmetry sectors, since

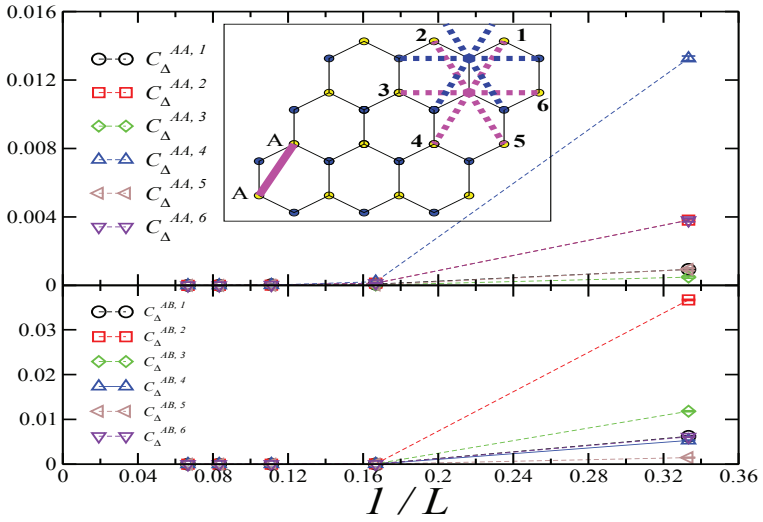

Supplementary Figure 10 | Finite size scaling of the next-nearest neighbour pair correlations $C_\Delta^{AA,j}$ and $C_\Delta^{AB,j}$ at $U/t = 4$. The inset illustrates the inequivalent directions with respect to the reference bond marked by AA, with the lower (upper) star corresponding to equal (different) sublattices. Error bars denote standard errors.

the full Cooper pair correlations $\langle \Delta_{ext.-s}(0)\Delta^\dagger_{ext.-s}(\mathbf{d}_L)\rangle$, $\langle \Delta_{p_x}(0)\Delta^\dagger_{p_x}(\mathbf{d}_L)\rangle$, $\langle \Delta_{p_y}(0)\Delta^\dagger_{p_y}(\mathbf{d}_L)\rangle$, $\langle \Delta_{d_{xy}}(0)\Delta^\dagger_{d_{xy}}(\mathbf{d}_L)\rangle$, $\langle \Delta_{d_{x^2-y^2}}(0)\Delta^\dagger_{d_{x^2-y^2}}(\mathbf{d}_L)\rangle$, and $\langle \Delta_f(0)\Delta^\dagger_f(\mathbf{d}_L)\rangle$ are linear superpositions of the above pair-pair correlation functions, and hence vanish in the thermodynamic limit. We can thus exclude superconductivity in the half-filled Hubbard model on the honeycomb lattice.

9 Lower bound for singlet states in the RVB phase

We consider the internal energy as a function of the projection parameter Θ,

$$E(\Theta) = \frac{\langle \Psi_T | \mathrm{e}^{-\Theta H/2} H \mathrm{e}^{-\Theta H/2} | \Psi_T \rangle}{\langle \Psi_T | \mathrm{e}^{-\Theta H} | \Psi_T \rangle} , \tag{36}$$

where $|\Psi_T\rangle$ is the trial wave function (cf. Methods). Let $\{|n\rangle\}$ be the set of eigenstates of H. Then, we have

$$E(\Theta) - E_0 = \frac{1}{1+R(\Theta)} \sum_{n>0} \mathrm{e}^{-(E_n-E_0)\Theta} (E_n - E_0) \frac{|\langle n|\Psi_T\rangle|^2}{|\langle 0|\Psi_T\rangle|^2} , \tag{37}$$

where E_0 is the ground-state energy, $|0\rangle$ the ground-state, and define

$$R(\Theta) = \sum_{n>0} \mathrm{e}^{-(E_n-E_0)\Theta} \frac{|\langle n|\Psi_T\rangle|^2}{|\langle 0|\Psi_T\rangle|^2} . \tag{38}$$

Next, we consider an energy scale

$$\epsilon \ll (E_1 - E_0)/N \ , \tag{39}$$

where E_1 is the energy of the first excited singlet with the same quantum numbers as the ground-state, and define Θ^*, such that for $\Theta > \Theta^*$, $(E(\Theta) - E_0)/N < \epsilon$. Typically, ϵ can be taken of the order of the statistical error in the energy, such that the condition on ϵ is clearly fulfilled. However, ϵ is not defined in terms of the statistical errors; the only defining condition on ϵ is (39). With such a definition we have

$$\epsilon = \frac{1}{N} \sum_{n>0} \frac{\mathrm{e}^{-(E_n - E_0)\Theta^*}}{1 + R(\Theta^*)} (E_n - E_0) \frac{|\langle n|\Psi_T\rangle|^2}{|\langle 0|\Psi_T\rangle|^2} \ll (E_1 - E_0)/N \ , \tag{40}$$

such that

$$\frac{R(\Theta^*)}{1 + R(\Theta^*)} < \sum_{n>0} \frac{\mathrm{e}^{-(E_n - E_0)\Theta^*}}{1 + R(\Theta^*)} \frac{(E_n - E_0)}{(E_1 - E_0)} \frac{|\langle n|\psi_T\rangle|^2}{|\langle 0|\psi_T\rangle|^2} \ll 1 \ , \tag{41}$$

so that it also holds that $R(\Theta^*) \ll 1$. The last inequality also implies that

$$\mathrm{e}^{-(E_1 - E_0)\Theta^*} \frac{|\langle 1|\Psi_T\rangle|^2}{|\langle 0|\Psi_T\rangle|^2} \ll 1 \ , \tag{42}$$

since the sum in $R(\Theta)$ consists of positive definite terms. In case the overlaps in the last inequality are finite,

$$(E_1 - E_0)\Theta^* \gg 1 \ , \tag{43}$$

such that $1/\Theta^*$ provides a lower bound for $E_1 - E_0$. In case $|\langle 1|\Psi_T\rangle|^2/|\langle 0|\Psi_T\rangle|^2 \ll 1$ such that the inequality (42) is fulfilled due to a vanishing overlap, we miss the lowest excited singlet state, and $1/\Theta^*$ provides a lower bound for the next lowest singlet with a finite overlap with the trial wave function.

For the determination of the lower bound for singlet states we concentrated on the value $U/t = 4$, centered in the RVB phase. We verified that in the case $L = 2$, where the system can be fully diagonalized, setting $\epsilon = 10^{-3}t$, $1/\Theta^* = (0.74 \pm 0.04)t$ (s.e.m.) is a lower bound. Namely, for this system size, $E_1 - E_0 = 1.84t$ for the first excited singlet state of momentum $\mathbf{k} = 0$. We also verified that this state has an overlap of 0.22 with the trial wave function. The above value of ϵ corresponds to the maximal error for all system sizes. The uncertainty in the determination of Θ^* is taken as the maximum between (i) the distance from Θ^* to the value of Θ for $E(\Theta)/N = E(\Theta^*)/N - \epsilon$ and (ii) the distance between two consecutive values of Θ around Θ^*. By means of error propagation, we then estimate the error in $1/\Theta^*$. In Suppl. Fig. 11 we display $1/\Theta^*$ for $L = 3$, 6, 9, and 12, and an extrapolation to the TDL. In all these cases, the lower bound is

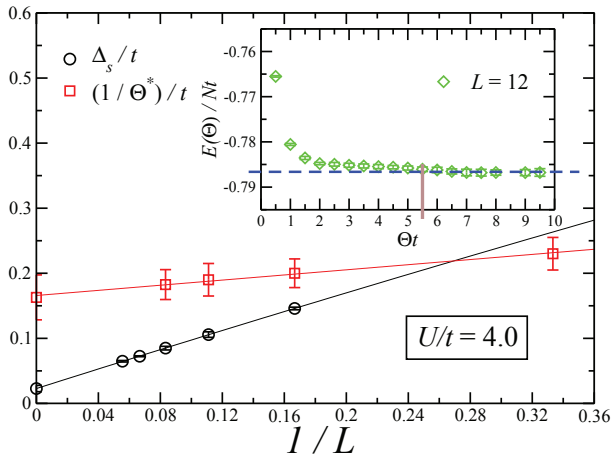

Supplementary Figure 11 | Lower bound $1/\Theta^*$ for $L = 3$, 6, 9, and 12 at $U/t = 4$. For comparison, the values of the spin-gap are reproduced. The inset shows the internal energy $E(\Theta)$ as a function of the projection parameter Θ for the $L = 12$ system. The vertical bar gives the position of Θ^*. Error bars in Δ_s and $E(\Theta)$ denote standard errors. For the determination of the error bars in $1/\Theta^*$, see the text.

above the spin-gap, as well as the extrapolation to the TDL. Hence, we find no evidence for singlet states with the same quantum numbers as the ground-state, that may become degenerate with it in the thermodynamic limit. However, this result does no exclude the possibility of low-lying singlet states that have vanishing overlaps with our trial wave function.